Applied Materials Today 21 (2020) 100869

Contents lists available at ScienceDirect

Applied Materials Today

journal homepage: www.elsevier.com/locate/apmt

Effect of semiconductor to metal transition on thermoelectric performance in oxide nanocomposites of $SrTi_{0.85}Nb_{0.15}O_3$ with graphene oxide

Pritam Dey, Subhra Sourav Jana, Farheen Anjum, Tathagata Bhattacharya, Tanmoy Maiti*

Plasmonics and Perovskites Laboratory, Department of Materials Science and Engineering, IIT Kanpur, U.P. 208016, India

ARTICLE INFO

Article history:
Received 6 June 2020
Revised 7 October 2020
Accepted 26 October 2020

ABSTRACT

Donor doped $SrTiO_3$ based perovskites are considered as very promising candidates for high temperature thermoelectric applications, but the figure of merit (ZT) of these n-type oxide thermoelectrics need to be enhanced for making it commercially viable. However, it is challenging to improve the transport properties of these oxides in order to achieve high ZT. Here we put forward a strategy of boosting the electron transport by inducing semiconductor to metal transition in Nb doped $SrTiO_3$ (STN) by formation of nanocomposites with graphene oxide (GO). We could enhance electrical conductivity remarkably by gradual incorporation of GO in the matrix of STN, which changed its semiconductor ($d\sigma/dT>0$) behavior into metallic ($d\sigma/dT<0$) for more than 1 wt% GO content. GO sheets embedded in the grain boundaries of polycrystalline STN facilitated electron transport without increasing much it's thermal conductivity, resulting in the order of magnitude increase in the ratio of electrical conductivity and thermal conductivity in the temperature range from 300 K to 1200 K. Hence, ZT of STN ceramics was raised by 50 times due to GO incorporation. Maximum ZT of 0.5 was attained at 1200K in n-type bulk oxide nanocomposite made of environmentally benign, earth-abundant elements.

1. Introduction

Electricity plays a major role in our everyday life. However, the available finite energy resources, need to be used in far more efficient manner compared to the current scenario in electronic appliances, combustion engines, manufacturing industries and power plants, where more than 60% of the energy is wasted as heat [1]. In this regard, thermoelectric material offers a better way of clean energy generation by recycling the waste heat without much environmental impact. Energy conversion efficiency of thermoelectric (TE) power generator depends on few influencing parameters, which are inter-related by dimensionless figure of merit, $ZT=S^2\sigma T/k$; where S, σ, T, k are Seebeck coefficient, electrical conductivity, temperature and thermal conductivity, respectively [1]. Over the last few decades, various TE materials such as Chalcogenides [2], Skutterudites [3], Chlathrates [4], Half- Heusler alloys [5] etc. were developed. However, these metal-based TE materials suffer from poor durability at high temperature, toxicity and low abundance of constituent elements. On the other hand, oxides can be stable at high temperature ($\geq$1000K) in oxidizing and corrosive environment. However, bulk oxides especially n-type thermoelectrics suffer from poor ZT values compared to metal-based systems. Among the various n-type oxide materials $SrTiO_3$ is most widely researched material system [6–15]. Nb is most widely used [6–9] as donor in Ti-site to increase the electrical conductivity of $SrTiO_3$, which is a band insulator. Adopting the strategy of using finer particles in order to obtain bimodal grain size distribution Tkach *et al.* reported ZT ~ 0.36 at 970 K [8]. Also, researchers used rare-earth element like La [10–13] in Sr-site to improve the ZT values. Use of both the donors Nb and rare-earth La in $SrTiO_3$ yielded ZT $\approx$0.6 at >1000K [14]. Incorporation of secondary phases [16] in the matrix of TE material was considered as a simple top down approach to improve ZT by enhancing the interfacial phonon scattering [17,18]. Carrier filtering effects at grain boundary and enhanced phonon scattering due to interfacial strain by grain boundary modification were reported as the possible mechanisms for ZT enhancement [18]. 2D materials like graphene, showed modification of strain at grain boundary [19] causing lower lattice thermal conductivity leading towards enhanced thermoelectric performance in graphene-based composites [20–24]. Using the strategy of making composite with graphene (G) or reduce graphene oxides (r-GO), over the past few years, researchers demonstrated ZT

* Corresponding author.
E-mail address: tmaiti@iitk.ac.in (T. Maiti).

https://doi.org/10.1016/j.apmt.2020.100869
2352-9407/

enhancement of pure $SrTiO_3$ [25], Nb [26,27] and La [28] doped or co-doped [29] $SrTiO_3$. These strategies of enhancing ZT values remained focused on the grain boundary modification by conductive G or r-GO to enhance electron transport. Lin *et al.* [28] first demonstrated 280% increase in ZT values due to graphene incorporation in La doped $SrTiO_3$ securing maximum ZT ~ 0.42 at room temperature for 0.6wt% graphene. They attributed ZT enhancement to the manifold increase in electrical conductivity due to the formation of a percolation network of graphene along with lower lattice thermal conductivity (κ_l) caused by the enhanced phonon scattering arising from the cluster of oxygen vacancies and the presence of flaky graphene at the grain boundary. Recently, Wu *et al.* [27] and Okhay *et al.* [26] observed the enhancement of ZT in 10% Nb doped $SrTiO_3$ by forming the composites with r-GO yielding the maximum ZT of 0.22 at 800K and 0.29 at 1160K, respectively. They attributed the reason behind large electrical conductivity of composites to the high electrical mobility and large carrier concentration due to r-GO induced reduction of oxide grains. Reduced κ_l was further explained by the enhanced phonon scattering due to the Sr and O vacancy caused by the presence of r-GO in the grain boundaries. Although these prior investigations [26,27] on composites of Nb doped $SrTiO_3$ with r-GO showed the signature of metal-semiconductor transition behavior in the temperature dependent electrical conductivity plot, such interesting phenomenon was hardly discussed.

In the present work, we synthesized $SrTi_{0.85}Nb_{0.15}O_3$ (STN) via spark plasma sintering (SPS) process, which we optimized earlier [30] and further modified its transport properties by synthesizing nanocomposites with graphene oxide (GO) instead of G or r-GO. Since GO is comparatively insulator in nature than G or r-GO it is worth investigating the effect of GO addition on both electron and heat transport in STN. It has also been reported [25] that occurrence of graphene or r-GO in the grain boundaries of $SrTiO_3$ oxide enables the reduction of Schottky barrier height in the grain boundaries as r-GO facilitates oxygen pumping out, resulting in excess oxygen vacancies at the vicinity of grain. That possibility can be ruled out in the present work since we have GO segregated along the grain boundaries, which is not expected to create the similar kind of reducing environment like r-GO in the vicinity of oxide grains. Interestingly, in our current investigation on nanocomposites of STN with GO, we could enhance the electrical conductivity 250 times compared to pure STN. In spite of using less conductive GO, such phenomenal increase in electrical conductivity was achieved by manipulating the semiconductor to metal transition temperature ($T_{S\text{-}M}$) of STN. We observed that the semiconductor behavior of pure STN could be changed into metallic at room temperature by incorporating GO in STN matrix. Trade-off between semiconducting and metallic nature of STN with optimum amount of GO led to phenomenal increase in electrical conductivity with little change in thermopower and thermal conductivity. Due to enhanced electron transport by GO incorporation in STN oxides without affecting much on its thermal conductivity, we could achieve 50 times increase in the ratio of electrical and thermal conductivity (σ/κ) at 1200 K resulting in enhanced ZT ~0.5 obtained for bulk oxide nanocomposite of STN with 1.5 wt% GO. To the best of our knowledge, this is the first report on ZT enhancement by manipulating $T_{S\text{-}M}$ of oxides. Our results thus open up new avenue of fabricating high temperature thermoelectric power generator for solid state electricity generation from waste heat.

2. Experimental

2.1. Processing of nano-composite

In our present work we developed an n-type oxide nanocomposite for which we chose $SrTiO_3$: 15at.% Nb (STN) as a matrix and graphene oxide (GO) as an inclusion in this ceramic matrix. STN+ x wt. % GO samples with x=0.0, 0.5, 1.0, 1.5 & 2.0were synthesized by Spark Plasma Sintering (SPS) route.

2.1.1. Synthesis of STN oxides

Initially the stoichiometric amount of precursors such as $SrCO_3$, TiO_2 and Nb_2O_5 were mixed using zirconia balls and ethanol as a medium in a roller ball mill for 24 h at 320–400 rpm. The thoroughly mixed and dried up powder was then kept for calcination at 1673–1800 K for 24 h in H_2 atmosphere. Calcination step was carried out multiple times until we got single-phase solid solution of $SrTi_{0.85}Nb_{0.15}O_3$.

2.1.2. Synthesis of Graphene oxide

There are many methods to convert graphite into graphene oxide. The Hummers method [31] had been the most widely used method though this method was modified a lot from the old method.

Using this Hummers and Offeman method [31] graphene oxide was made by mixing the potassium permanganate ($KMnO_4$) into the slurry of graphite, sulphuric acid (H_2SO_4) and sodium nitrate ($NaNO_3$). The balanced equation of the reaction is written below.

$$KMnO_4 + H_2SO_4 = K^+ + [HMnO_4] + HSO_4^-$$

$$2HMnO_4 = Mn_2O_7 + H_2O$$

$$2NaNO_3 + H_2SO_4 = Na_2SO_4 + 2HNO_3$$

$$Mn_2O_7 + 2H_2SO_4 = [MnO_3] + [HSO_4]^- + H_2O$$

Dimanganeseheptoxide (Mn_2O_7) was formed from the reaction of potassium permanganate ($KMnO_4$) and sulphuric acid (H_2SO_4). The in-situ compound dimanganeseheptoxide (Mn_2O_7) is a far better oxidizer than potassium permanganate; dimanganeseheptoxide (Mn_2O_7) decomposed into manganese oxide (MnO_2) and nascent oxygen (O^-), which is highly reactive.

The graphite powder (1 gm) and sodium nitrate (0.5 gm) were taken into a 400 ml beaker in 2:1 ratio and mixed well on an ice-water bath to maintain 20°C temperature on a magnetic stirrer. Subsequently 23 ml conc. Sulphuric acid was added dropwise with simultaneous stirring and 3 gm potassium permanganate was added slowly.

After 20 mins, ice-water was removed; subsequently the beaker was heated at 35°C for 30 mins and 46 ml DI water was added and kept at 90°C again for further 30 mins. And then 40 ml warm DI water was added and finally 30% H_2O_2 (aq) was added until the bubbling disappeared resulting the yellow solution.

It was filtered through Whatman 40 filter paper and warm DI water was used to decrease it's pH from the acidic range. The thick slurry was then dispersed in warm DI water (<55°C) by ultrasonication for 30 min and subsequently centrifuged at 5500 rpm for 20 mins each time until the pH 7 was reached. The recovered thick slurry was then lyophilized to get dark brown coloured graphite oxide flakes. 10 mg of the lyophilized graphite oxide flakes were taken into a 200 ml RBF with 100 ml warm DI water. The solution was then ultrasonicated for about 120 min until no particles were observed, resulting beautiful brown coloured solution of graphene oxide. The solution was re-centrifuged at 7000 rpm for 25 min and the thick slurry of graphene oxide was vacuum dried at 50°C for 6 h.

2.1.3. Synthesis of STN+GO nano-composite

The calcined STN powder was mixed with various weight % of GO and further milled using a planetary micro mill (Fritsch®, PULVERISETTE 7 premium Line, Rhineland-Palatinate, Germany) for

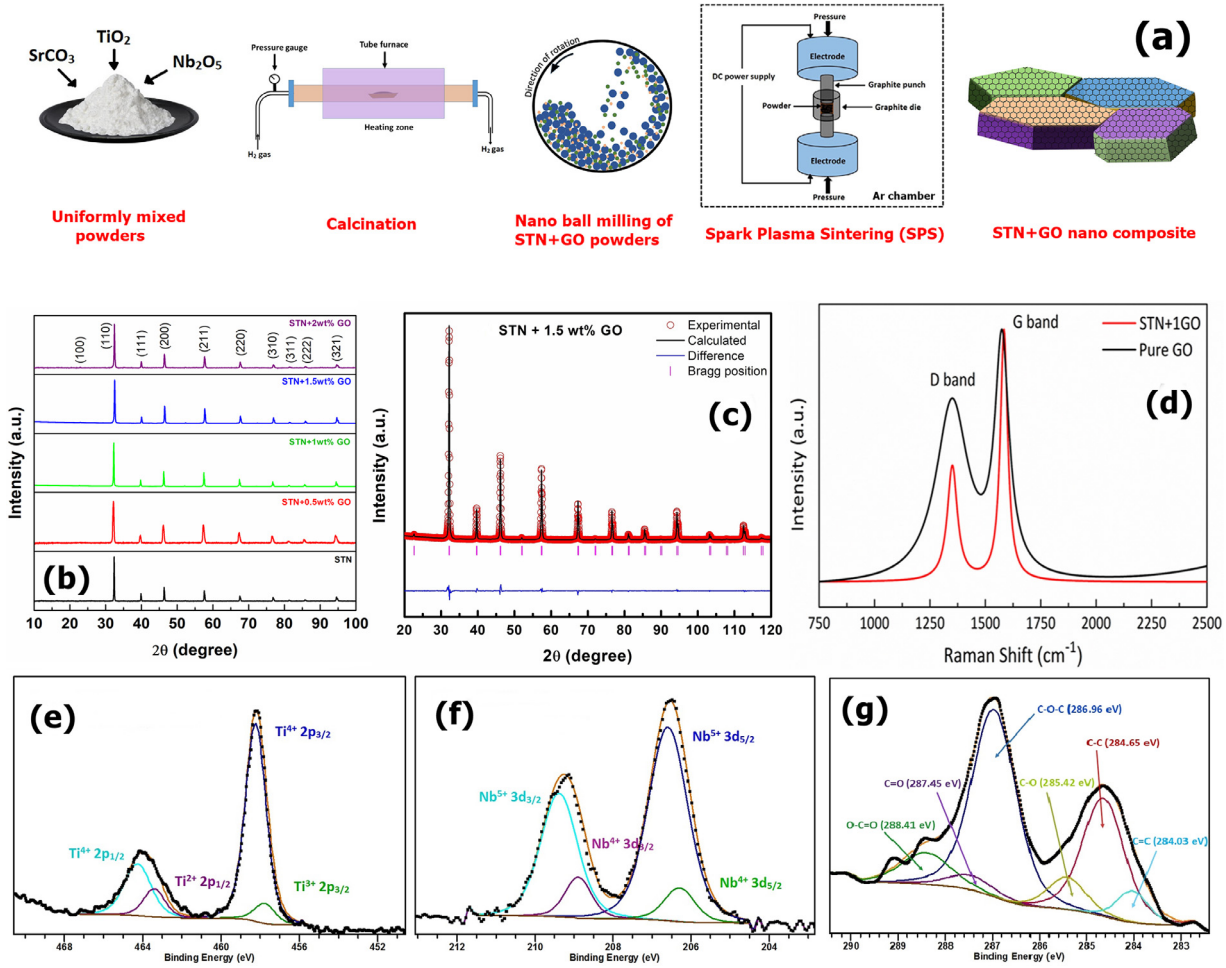

Fig. 1. **(a)** Schematic of the synthesis process of STN-GO nanocomposite **(b)** XRD patterns of STN+x wt% GO composites with x =0.0, 0.5, 1, 1.5 & 2. **(c)** Rietveld refinement of STN+1.5wt% GO, **(d)** Raman spectra of STN+1wt.% GO composite pellet and pure GO flakes. **(e-g)** represents the XPS results of Ti 2p, Nb 3d and C 1s peak respectively, for STN+1.5wt% GO sample.

90–150 mins at 600–800 rpm using zirconia grinding balls. The powder mixture was then sintered with SPS (El Tek Co., Korea) at 1600-1700 K temperature and 30–50 MPa pressure for 5–7 min using cylindrical graphite die of 15 mm diameter in Argon atmosphere at a heating and cooling rate of 200°C/min and 50°C/min respectively.

2.2. Material characterization

The thermoelectric measurements (electrical conductivity and Seebeck coefficient) of these composites were carried out from room temperature to 1223 K at the interval of 50 K and ΔT of 20K, 30K and 40K using a ZEM3-M10 apparatus (ULVAC-RIKO Inc.). Thermal diffusivity (D) was measured by laser flash technique using LAF 1000 Linseis (Germany) and specific heat of these composites were measured by Differential Scanning Calorimeter (DSC, 404 F3, Netzsch, Germany) from room temperature to 1223K to calculate the thermal conductivity ($\kappa = C_p.\rho.D$).

Crystal structure and phase identification of these sintered composites were first tried to investigate by X-ray diffraction technique using PAN analytical Empyrean X-ray diffractometer. Raman scattering spectra on the polished surface of these sintered composites were collected at room temperature by linearly polarized output of solid state laser of 532 nm using Princeton instrument Acton series SP 2500i spectroscope. XPS spectra of these samples were measured using Al-Kα radiation (1486.6 eV) for excitation source in PHI 5000 Versaprobe II and the binding energies were calculated with respect to adventitious carbon, 284.8 eV. FESEM images and Energy-dispersive X-ray spectra (EDXS) were collected on the fractured surface using JSM-7100F, JOEL. Further microstructural studies were carried out to investigate the distribution of GO in these composites using high-resolution transmission electron microscopy in FEI Titan G2, HRTEM, where the inverse FFT data analysis of HRTEM was done by GATAN software.

3. Result and discussion

3.1. Structure, microscopy and spectral investigation

Composites of STN+ x wt. % GO (x=0, 0.5, 1, 1.5 and 2) were synthesized by solid state reaction route using Spark Plasma Sintering (SPS) as shown schematically in Fig. 1(a). No secondary phases were detected in the XRD profiles as all the reflections were indexed with respect to cubic perovskite structure shown in Fig. 1(b). Rietveld refinement of XRD data verified the symmetry of these compounds as $Pm\bar{3}m$ space group as shown in Fig. 1(c). Refinement parameters are given in Table S1 (Supporting Information). High temperature XRD of these ceramics confirmed that it retained the cubic structure without appearance of any extra phase as shown in Fig. S1 (Supporting Information). Moreover, it validates that these compounds are stable in the temperature range from 300 K to 1173 K. Evidence of GO could not be found in the

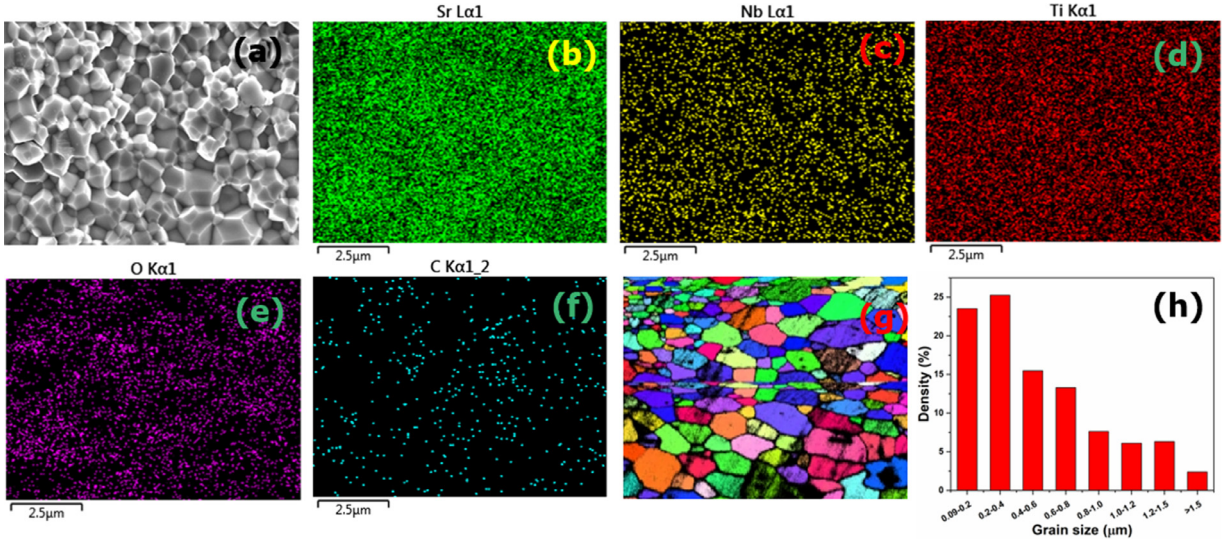

Fig. 2. **(a)** FESEM micrograph, **(b-f)** elemental color mapping of Sr, Nb, Ti, O & C by Energy-dispersive X-ray diffraction (EDXS) and **(g-h)** EBSD image of STN+ 1.5wt% GO sample and the grain size distribution bar chart.

XRD pattern possibly due to limit of the instrument to detect small amount of GO present in STN matrix.

To confirm the existence and purity of GO in our nanocomposites, 532 nm Raman spectra were collected for as-synthesized GO and STN+GO composites depicted in Fig. 1(d). Raman spectra G band, which is the signature of phonon Eigen vector E_{2g} due to first order phonon scattering of sp^2 carbon atoms [32] was found at 1584 cm^{-1} for pure GO as well as in STN+GO composites. Besides, D band Raman spectra appeared at 1351 cm^{-1} due to K point phonons of A_{1g} symmetry [32] in both GO and composite samples. The reduction in the I_d/I_g value observed in the Raman spectrum of STN+1GO composite compared to that of pristine GO can be attributed to the increase in individual crystallite size of sp^2 domains. [33]

Elemental composition and functional groups of these nanocomposites were detected by XPS. The fitted XPS spectra of Ti2p, Nb3d and C1s are displayed in Fig. 1 (e-g) and binding energies are presented in Table S2 (Supporting Information). It is evident that both Ti and Nb were present in multiple oxidation states in these ceramics. The ratio of the calculated area under Ti^{3+} and Ti^{4+} XPS peaks determined from the fitting of Ti2p XPS spectra was found to be 15.6: 84.4, suggesting that almost 85% of Ti possessed 4+ oxidation state. Similarly, investigation of Nb3d spectra suggests the presence of 14.7 % Nb^{4+} and 85.3% Nb^{5+}. The C 1s XPS spectrum showed the presence of 28% carbon as non-oxygenated Csp^3 (C-C) and 5.6% as Csp^2 (C=C) at 284.65 eV and 284.03 eV, respectively. Moreover, ~47% carbon was found to form epoxy (C-O-C) group (286.96 eV) besides the presence of other oxygen-containing functional groups of carbon such as hydroxyl (C-O), epoxy (C-O-C), carbonyl (C=O), carboxylate (O–C=O), suggesting the presence of GO in the oxide nanocomposites, which further corroborates with the analysis of Raman spectra.

FESEM of STN+GO samples confirmed the existence of dense sub-micron level grains in these composites with no such porosity in microstructure as shown in Fig. 2(a). Also the elemental color mapping carried out by EDXS shown in Fig. 2 (b–e) confirmed the homogeneous distribution of constituting elements (Sr, Ti, Nb, O) in STN+GO samples. However elemental mapping of C shown in Fig. 2(f) suggests that distribution of GO is sparse indicating possible segregation along the grain boundaries. Furthermore, we estimated the grain size distribution using Electron Back Scattered Diffraction (EBSD) shown in Fig. 2(g-h). To achieve high ZT values, we need an optimum grain size distribution balancing nano-size grains required for low lattice thermal conductivity as well as micron-size grains for obtaining good electrical conductivity. It can be seen from Fig. 2(h) that micron-size grains (>1.5 μm) as well as small nm-size grains (<100 nm) were obtained in our nanocomposites. All the grains were found to be randomly oriented as expected in polycrystalline material. Most importantly, 24% grains obtained in STN+GO composites have the average diameter of less than 200 nm and almost 50 % grains have <400 nm average diameter. Such low grain size with different orientation is helpful in scattering phonons extensively.

The distribution of GO in the composite was further investigated by high resolution TEM. HRTEM image of grain boundary triple junction shown in Fig. 3(a) demonstrates that d-spacing of dark areas in grain boundary is around ~ 4.2 Å which corresponds to GO as reported in the literature. [34,35] Also, d-spacing in the range from 1.7 Å to 2.7 Å corresponds with different orientation of planes in STN perovskite were detected, which were further verified from XRD as well. Inter-planar spacing revealed that GO sheets were mostly embedded in the grain boundaries, although evidence of little GO inside the grain near grain boundary was also obtained. Furthermore, we carried out the high angle annular dark-field imaging (HAADF) of the nanocomposite sample shown in Fig. 3(b). It reveals that distribution of Sr, Ti, Nb and O is dense and uniform throughout the grains except grain boundary, which is evident from the black line representing grain boundary in the elemental mappings. Furthermore, we did elemental analysis by a line scan across the grain boundary shown in the inset of Fig. 3(b). It reconfirms that the grain boundaries are carbon-rich as GO segregated along the grain boundaries.

3.2. Thermoelectric property

3.2.1. Electronic property

Temperature dependent Seebeck coefficient and electrical conductivity are measured from 300 K to 1223 K for all the STN+GO composites and details of the measurement is given in the literature [36]. The negative thermopower values as evident in Fig. 4 (a) throughout the temperature range suggests that these materials are n-type, which can be explained by generation of electrons due to incorporation of Nb^{5+} in Ti^{4+}-site of $SrTiO_3$ perovskite as

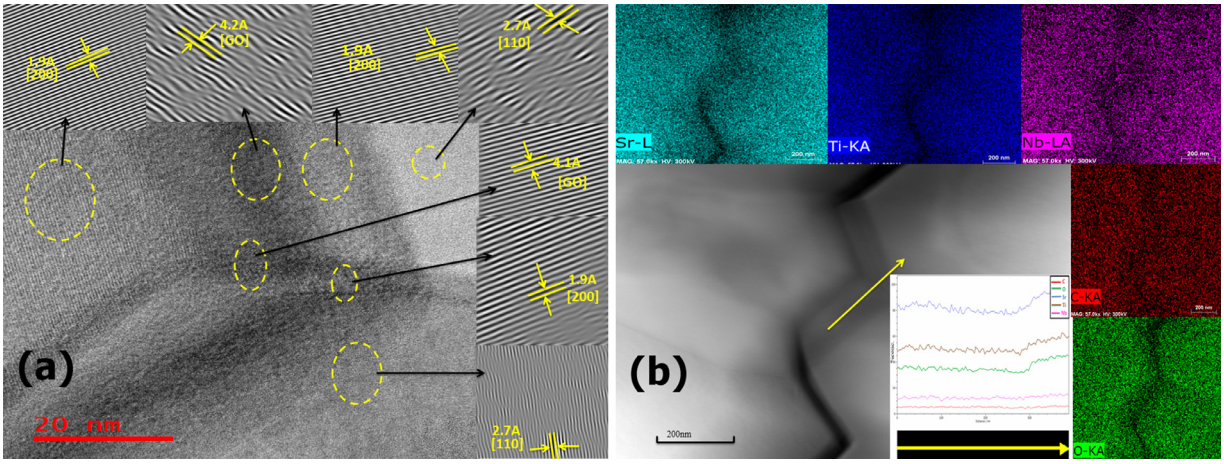

Fig. 3. **(a)** HRTEM images of STN+ 1.5 wt% GO composite taken at grain boundary triple junction and **(b)** HAADF-STEM imagine and EDS elemental mapping around the grain boundary region.

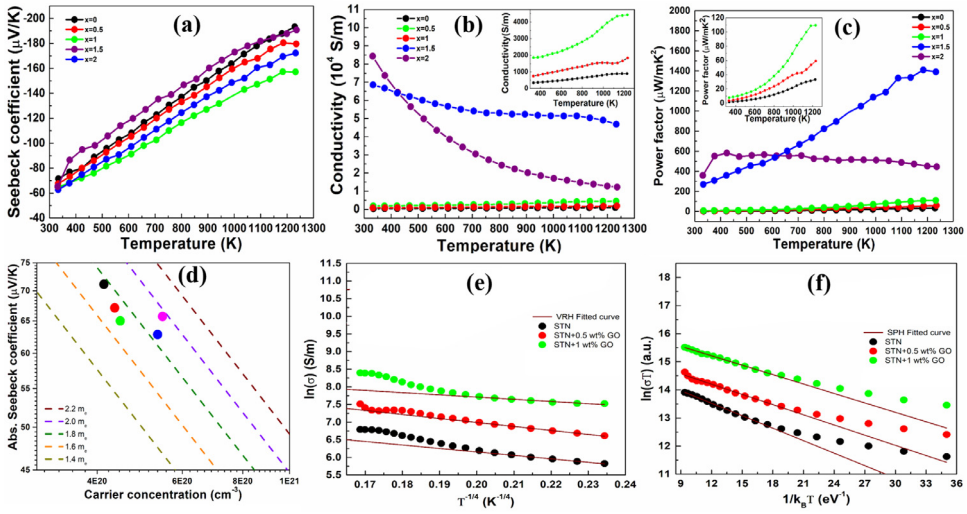

Fig. 4. **(a)** Seebeck coefficient (S), **(b)** Electrical conductivitiy (σ), **(c)** power factor, (**d**) Pisarenko plot **(e)** Variable range hopping (VRH) **(f)** Small polaron hopping (SPH) model in STN +GO samples.

expressed by following defect reaction.

$$4SrO + 2TiO_2 + Nb_2O_5 \rightarrow 4Sr_{Sr}^{\times} + 2Ti_{Ti}^{\times} + 2Nb_{Ti}^{\bullet} + 12O_O^{\times} + \frac{1}{2}O_2 + 2e' \quad (1)$$

Presence of majority of the niobium in 5+ oxidation state in these materials validated by XPS corroborates with the defect reaction (1).

Room temperature Seebeck coefficient decreased due to incorporation of GO in STN ceramics. However, Seebeck coefficient values increased continuously with increasing temperature for all the compositions suggesting degenerate semiconductor-like behavior. It is to be noted that the decrease in Seebeck coefficient due to GO addition is much smaller compared to the order of magnitude increase in electrical conductivity observed in these composites as shown in Fig. 4(b). Due to incorporation of small amount ($\leq$2 wt%) of GO in STN15 matrix, electrical conductivity increased more than 250 times from 338 S/m for pure STN15 to 85,000 S/m for STN-2GO composite. Carrier concentration (n) for these composites was estimated at room temperature from Hall measurement as shown in Table S3. It is evident from Table S3 that the electron concentration did not change much due to GO incorporation in STN15 although the trend was found to be increasing in the range (4.2 – 4.8) x 10^{20} cm^{-3}. Furthermore, we calculated the density of states effective mass from Pisarenko Eq. (2).

$$S = \frac{8\pi^2 k_B^2}{3eh^2} m^* T \left(\frac{\pi}{3n}\right)^{2/3} \quad (2)$$

The estimated effective mass, shown in Fig. 4(d), changed very little with increasing GO content in the composites, dwelling between 1.8 m_e and 1.9 m_e, which is similar to what was reported earlier on STN with nano-inclusion. [37,38] It is apparent that incorporation of GO in the STN ceramics did not alter its carrier concentration and effective mass significantly. As a result, not much change in Seebeck coefficient was observed in the composite samples. However, GO sheets segregated in the grain boundary regions of polycrystalline STN ceramics improved its electron mobility (μ) causing the increase in electrical conductivity ($\sigma = ne\mu$). Since carrier mobility, $\mu = \frac{e\tau}{m^*}$, where τ is the relaxation time; it can be concluded that GO sheets embedded on the grain boundaries, which are considered as 2D defects, helped in the transport of electrons across the grain boundaries resulting higher relaxation time.

Enhancement of electrical conductivity due to GO addition can be somewhat predicted, as electrical conductivity of GO is higher than STN15 ceramics. But in order to understand such a remark-

able (250 times) increase in electrical conductivity obtained in STN+GO composites, one needs to evaluate its temperature dependent conductivity graph shown in Fig. 4(b). Electrical conductivity for pure STN15 changed from 338 S/m at room temperature to 888 S/m at 1230K demonstrating semiconducting ($d\sigma/dT>0$) behavior throughout the measurement temperature range (300K – 1200K). Upon GO incorporation in the STN matrix, the electrical conductivity retained its semiconducting ($d\sigma/dT>0$) nature up to 1 wt% GO shown in inset of Fig. 4 (b), although conductivity values increased manifold with increasing the amount of GO. With further increase in GO content, there is a stark change observed in the temperature dependent conductivity pattern. Instead, conductivity of 1.5 wt% and 2 wt.% GO compositions was found to be decreased with increasing temperature, inferring semiconductor ($d\sigma/dT>0$) to metal ($d\sigma/dT<0$) transition in STN+GO composites.

However, more insights can be gained by looking closely at their slope of σ vs T curve. The conductivity decreased with temperature in a much sharper manner in 2 wt% composition compared to 1.5GO. Due to the smaller slope of the σ vs T graph obtained in STN1.5GO composite, the conductivity values spanned in the range from 68540 S/m at 300 K to 46866 S/m at 1234 K. Such high conductivity values obtained in the wide range of temperature resulted enhanced thermoelectric power factor in this STN+1.5 wt% GO nanocomposite as shown in Fig. 4(c). The maximum power factor of 1410 μW/mK^2 at 1184 K was observed for STN+1.5 wt.% GO sample, which is more than 40 times higher than that obtained in pure STN15 (≈33.21 μW/mK^2 at 1234 K).

The enhancement in electrical conductivity of polycrystalline STN due to incorporation of graphene or r-GO in the prior reports [26,27] has been attributed to the reduction of oxide grains. Rahman *et al.* [25] have explained this incredible phenomenon of electrical transport by generation of Schottky barrier, which is quite common for polycrystalline ceramics due to depletion in oxygen vacancy near grain boundary. They [25] have reported that occurrence of graphene or r-GO in the grain boundaries of $SrTiO_3$ could effectively reduce the Schottky barrier height in the grain boundaries as r-GO facilitates oxygen pumping out resulting in excess oxygen vacancy at the vicinity of grain boundary. In our present composite system of STN+GO, enhancement of electron mobility and electrical conductivity suggests the reduction of the Schottky barrier height in polycrystalline ceramics. However, it is questionable if GO is capable of producing great deal of oxygen vacancy similar to r-GO. As confirmed in our XPS since GO consists of out of plane carbon-oxygen bond (in the form of hydroxyl (C-O), epoxy carbonyl (C-O-C) and carboxylate (O-C=O) groups) which are particularly absent in r-GO, it is not likely to produce same reducing atmosphere like rGO. However, some amount of oxygen vacancy generation near grain boundary (resulting reduction in Schottky barrier height) cannot be completely ruled out. Hence it is difficult to assimilate that 250 times surge in electrical conductivity observed in STN due to GO incorporation is solely because of oxygen vacancy generation. It is also unable to explain why there is almost no change in Seebeck coefficient after GO addition in STN despite phenomenal increment in electrical conductivity on the contrary to r-GO incorporated pure $SrTiO_3$ where conductivity enhancement occurred at the expense of decrease in Seebeck coefficient [25]. Further, the striking change in the conductivity slope from semiconductor ($d\sigma/dT>0$) to metal-like ($d\sigma/dT<0$) behavior with increase in GO content has never been observed in earlier reports on doped $SrTiO_3$ based composites with r-GO or graphene.

Perovskite materials with high carrier concentrations, have been reported to demonstrate charge transport behavior governed by complex processes such as adiabatic small polaron hopping and localized Anderson-variable hopping [39]. Interestingly, Bijaalie *et al.* [40] have shown that donor doped $SrTiO_3$ can behave like a Mott insulator instead of acting like a heavily doped semiconductor due to strong electron-electron interaction and lattice distortion (strain).

Semiconductor to metal transition (S-M), which was found to be responsible for remarkable improvement of electrical conductivity in STN+ GO composites, was previously reported for wide range of materials including perovskite based oxides [10,39,40]. Such S-M transition is often described as Mott transition when the following criteria is satisfied

$$a_B n^{\frac{1}{3}} \approx 0.25 \tag{3}$$

where, $a_B$is Bohr radius and n is critical carrier concentration. Critical carrier concentration in $SrTiO_3$ was found to be on the order of 10^{18} cm^{-3} [10,40]. In our Nb doped $SrTiO_3$ system carrier concentration was estimated by Hall measurement on the order of 10^{20} cm^{-3}, which is expected to be much higher than that required for Mott transition. Interestingly, even though the carrier concentration satisfies the Mott criteria, STN+GO composites with ≤1 wt% GO didn't exhibit S-M transition. It can be explained by the Anderson transition, which is a charge localization phenomenon due to local strain and electric fields. The presence of multivalent cations (Ti^{4+}/Ti^{3+} and Nb^{5+}/Nb^{4+}) is expected to create a variation in local electric field and point defects giving rise to the lattice distortion in these composites, which causes Anderson transition. In the STN+GO composites with ≤ 1 wt% GO the Anderson localization was so dominant that carriers were trapped preventing them to exhibit metallic behavior. However, with a little increase in GO content the metallic behavior was observed in the STN+GO composites with ≥1.5 wt. % GO. Although we need further theoretical and experimental evidences to fully understand such S-M transition, the shift in S-M transition temperature ($T_{S\text{-}M}$) can be explained by lattice strain in analogy with nickel-based perovskites. Stability of metallic states by lattice strain was previously reported in rare earth nickelates ($RNiO_3$) by various researchers [41–43]. Presence of GO in the grain boundary is expected to create a compressive strain field around STN grains, which can be attributed to the reason behind instillation of metallic behavior beyond a certain amount of GO in STN+GO composites.

Since charge carriers are localized in the defect sites causing an energy barrier, charge transport mechanism in these oxides is generally governed by hopping conduction mechanism. Here, we fitted the conductivity data with variable range hopping (VRH) [44,45] and small polaron hopping (SPH) [46,47] model as descried by Eqs. (4) and (5), respectively.

$$\sigma = \sigma_o exp\left[-\left(\frac{T_o}{T}\right)^{1/4}\right] \tag{4}$$

$$\sigma = \frac{\sigma_o}{T}\exp\left(\frac{-E_{hop}}{kT}\right) \tag{5}$$

Where σ_o, $T_o$are constants, E_{Hop} is activation energy for SPH, and k_B is Boltzmann constant. In STN+GO compositions $x = 0,\ 0.5$ and 1, which demonstrated semiconductor like behavior, we observed that VRH model was followed up to a temperature, beyond which the conduction mechanism was found to be governed by SPH as shown in Fig. 4(e & f), respectively. The activation energy (E_{Hop}) required for small polaron hopping was found to be decreased with increasing GO content as shown in Table S4 (Supporting information). It further corroborates well with increasing conductivity observed with increasing GO. Also, in our STN+GO nanocomposites the grain boundary oxygen diffusion kinetics is expected to be changed due to presence of GO in the grain boundaries causing impact on electron mobility. Better kinetics of oxygen diffusion in grain boundaries indeed facilitate the electron hopping across the grain boundary. As a result, we have observed gradual decrease in activation energy barrier for small polaron hopping with increase in GO content. It can be concluded that stacks of 2D GO sheets em-

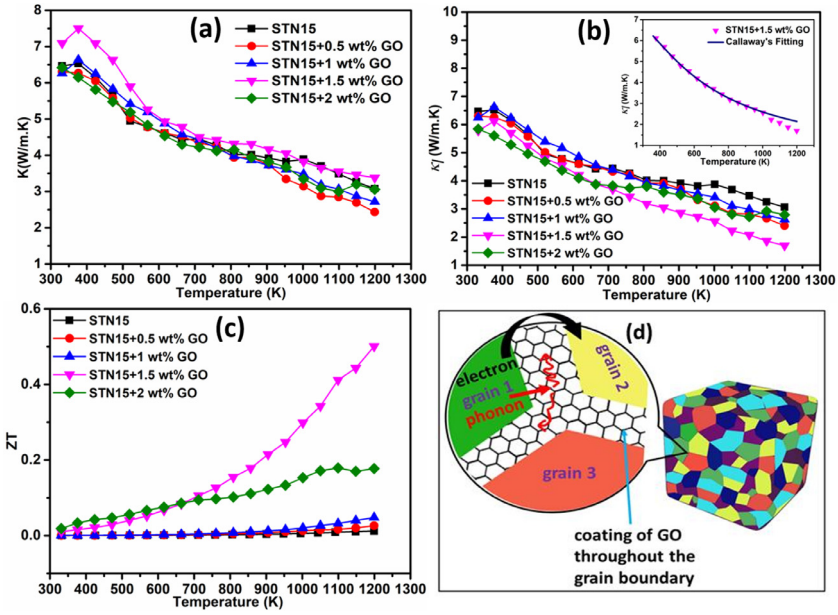

Fig. 5. Temperature dependent **(a)** total thermal conductivity (κ), **(b)** lattice thermal conductivity (κ_l) and Callaway model fitting for 1.5 wt% GO composition in Inset. **(c)** figure-of-merit, ZT and **(d)** schematic representation of the grapheme oxide (GO) in grain boundary acting as a sieve to filter phonons but passing electrons.

bedded over the grain boundary of these materials facilitated the electron hopping across the grain boundary as shown schematically in Fig. 5 (d). However, beyond a threshold limit of GO i.e. x>1.5 in the present study STN+GO composites started showing degenerate semiconductor like behavior suggesting no energy barrier for electron transport.

3.2.2. Thermal property

Thermal conductivity of these composites was found to be decreased with increasing temperature from 300 K to 1200 K as shown in Fig. 5(a). However, the change in the thermal conductivity due to GO addition did not occur in large amount unlike electrical conductivity. Since we could manage to increase electrical conductivity (σ) 250 times without altering its thermal conductivity (κ) much, there is almost 3 orders of magnitude increase in the ratio of electrical to thermal conductivity (σ/κ) at room temperature due to GO inclusion as shown in Fig. S5 in Supporting Information. Even at high temperature e.g. at 1200 K we could enhance the (σ/κ) ratio by 50 times by forming composites with GO. We also calculated the electronic contribution of thermal conductivity (Fig. S4 in Supporting Information) for these composites using Wiedemann Franz law, $\kappa_e = L\sigma T$, where L is the Lorentz number [48]. We can conclude from magnitude of the lattice thermal conductivity (κ_l), shown in Fig. 5(b), that the majority of heat transport in these materials is governed by the lattice vibrations or phonons. The temperature dependent lattice thermal conductivity (κ_l) of these composites exhibits monotonic decreasing trend with temperature, which suggests the dominance of Umklapp scattering besides the additional phonon scattering caused by the GO network at the grain boundaries [23,28,49]. Further we analyzed the thermal conductivity using Callaway's model [50], which could be expressed as,

$$\kappa_l = \frac{k_B}{2\pi^2 v}\left(\frac{k_B T}{\hbar}\right)^3 \int_0^{\theta_D/T} \frac{\tau(y,T)y^4 e^y}{(e^y-1)^2}dy \tag{6}$$

Where $y=\hbar\omega/k_BT$, ω is the phonon frequency, $\hbar$ is the reduced Plank constant, θ_D is the debye temperature, v is the acoustic velocity and τ is a relaxation time. Relaxation time (τ) has contributions from grain boundary scattering (τ_B), point defect scattering(τ_{PD}), phonon-phonon Umklapp scattering(τ_U) and electron phonon scattering(τ_{ep}) as represented by Eq. (7). [51,52]

$$\tau^{-1} = \tau_B^{-1} + \tau_{PD}^{-1} + \tau_U^{-1} + \tau_{ep}^{-1} = \frac{v_m}{L} + A\omega^4 + B\omega^2 T exp\left(\frac{-\theta_D}{nT}\right) + C\omega^2 \tag{7}$$

Here, v_m is the mean acoustic velocity, L is the average grain size, θ_D is the Debye temperature and A, B and C are fitting parameters corresponding to the point defects, Umklapp process and electron phonon scattering, respectively. Debye temperature (θ_D) of all the compositions was determined with the help of mean acoustic velocity as discussed in the Supporting information (Table S5). Normal process of scattering was neglected here for simplicity. Also, grain boundary scattering was not taken into consideration since it is not the dominant mechanism at high temperatures as suggested by Casimir[53]. Further we estimated that point defect has less than 0.1% contribution to the total lattice thermal resistivity even at room temperature using the following expression [54,55].

$$R_l^{th} = R_{PD} + R_U + R_{ep} \tag{8}$$

Where, $R_l^{th} = (\frac{1}{\kappa_l})$ is the lattice thermal resistivity and R_{PD}, $R_U$and R_{ep} are thermal resistivity coming from point defect, Umklapp and electron phonon scattering.

$$R_{PD} = \frac{4\pi^2 V_o \theta_D \Gamma}{h v_m^2},\ R_U = \frac{\pi v_m h B T}{\theta_D k_B{}^2} \text{and } R_{ep} = \frac{\pi v_m h C}{\theta_D k_B{}^2} \tag{9}$$

Here, V_o is the average volume per atom in the crystal and Γ is related to the isotopic phonon scattering factor [56].

In our present STN+x wt% GO system, we fitted our lattice thermal conductivity (κ_l) data with Callaway's model considering Umklapp & electron-phonon scattering shown in Fig. 5(b) inset. It could be seen from the fitting parameters B and C tabulated in Table S6 for all the STN15+GO compositions that the B parameter, which is the characteristic of Umklapp scattering increased with GO content suggesting the decrease in lattice thermal conductivity due to the increased phonon-phonon scattering. Further, the C parameter which correlates the electron-phonon interaction was found to be

independent of GO content in our composites. A plausible explanation of decreasing lattice thermal conductivity with increasing GO content is that the network of GO is indeed acting as phonon scattering center by introducing further anharmonicity in the STN matrix. So effectively in our STN+GO composites, GO embedded in the grain boundaries acts as a membrane, which hinders the phonon transport but helps in electron hopping. A schematic view of electron and phonon transport through the GO layer is shown in Fig. 5(d). The variations of both electrical and thermal conductivity with GO loading in STN+GO composites are depicted in Fig. S6, which clearly shows that in spite of remarkable increase in electrical conductivity due to GO incorporation in STN matrix, we could restrain the increase in thermal conductivity. As a result, we could enhance thermoelectric figure of merit, ZT of STN+GO composites compared to pure STN oxide as shown in Fig. 5(c). Maximum ZT≈0.5 at 1200K was obtained for STN-1.5GO composition, which is 50 times higher than that of pure STN oxide.

4. Conclusion

In conclusion, we demonstrated that engineering semiconductor-metal transition of $SrTi_{0.85}Nb_{0.15}O_3$ (STN) by incorporating GO, we could increase the electrical conductivity 250 times more than pure STN ceramics without much impact on Seebeck coefficient (S) and thermal conductivity (κ). As a result, we could improve ZT values 50 times in environmentally benign, rare-earth free STN+GO oxide bulk thermoelectric nanocomposite resulting in maximum ZT~0.5 at 1200 K. Furthermore, our strategy of manipulating semiconductor to metal transition temperature by synthesizing nanocomposites in order to aid the effective transport of charge carriers in bulk perovskites, which are otherwise suffered from Anderson's localization is expected to pave the way for designing novel oxide materials for fabricating next generation high temperature thermoelectric power generator.

Author statement

T.M. was responsible for the original research concept, design of experiments and physical interpretation. P.D., F.A. and T.B. helped in synthesis of materials. S.S.J., T.B. and P.D. characterized the samples. F.A. was responsible for TEM of the samples. P.D. and S.S.J analyzed the data and wrote the main manuscript with the help of T.M. All authors reviewed the manuscript.

Declaration of Competing Interest

The authors declare no conflict of interest.

Acknowledgment

This work is supported by the grant from Science and Engineering Research Board, DST (SERB-DST), India (Grant No: IMP/2018/000955).

Supplementary materials

Supplementary material associated with this article can be found, in the online version, at doi:10.1016/j.apmt.2020.100869.

Reference

[1] J. He, M.G. Kanatzidis, V.P. Dravid, High performance bulk thermoelectrics via a panoscopic approach, Mater. Today 16 (5) (2013) 166–176.
[2] R.J. Mehta, Y. Zhang, C. Karthik, B. Singh, R.W. Siegel, T. Borca-Tasciuc, G. Ramanath, A new class of doped nanobulk high-figure-of-merit thermoelectrics by scalable bottom-up assembly, Nat. Mater. 11 (3) (2012) 233.
[3] G. Nolas, D. Morelli, T.M. Tritt, Skutterudites: A phonon-glass-electron crystal approach to advanced thermoelectric energy conversion applications, Annu. Rev. Mater. Sci. 29 (1) (1999) 89–116.
[4] G. Nolas, J. Cohn, G. Slack, S. Schujman, Semiconducting Ge clathrates: Promising candidates for thermoelectric applications, Appl. Phys. Lett. 73 (2) (1998) 178–180.
[5] C. Fu, S. Bai, Y. Liu, Y. Tang, L. Chen, X. Zhao, T. Zhu, Realizing high figure of merit in heavy-band p-type half-Heusler thermoelectric materials, Nat. Commun. 6 (2015) 8144.
[6] N. Wang, H. Chen, H. He, W. Norimatsu, M. Kusunoki, K. Koumoto, Enhanced thermoelectric performance of Nb-doped SrTiO 3 by nano-inclusion with low thermal conductivity, Sci. Rep. 3 (2013) 3449.
[7] B. Zhang, J. Wang, T. Zou, S. Zhang, X. Yaer, N. Ding, C. Liu, L. Miao, Y. Li, Y. Wu, High thermoelectric performance of Nb-doped SrTiO 3 bulk materials with different doping levels, J. Mater. Chem. C 3 (43) (2015) 11406–11411.
[8] A. Tkach, J.O. Resende, K.V. Saravanan, M.E. Costa, P. Diaz-Chao, E. Guilmeau, O. Okhay, P.M. Vilarinho, Abnormal grain growth as a method to enhance the thermoelectric performance of Nb-doped strontium titanate ceramics, ACS Sust. Chem. Eng. 6 (12) (2018) 15988–15994.
[9] A.V. Kovalevsky, M.H. Aguirre, S. Populoh, S.G. Patrício, N.M. Ferreira, S.M. Mikhalev, D.P. Fagg, A. Weidenkaff, J.R. Frade, Designing strontium titanate-based thermoelectrics: insight into defect chemistry mechanisms, J. Mater. Chem. A 5 (8) (2017) 3909–3922.
[10] T. Okuda, K. Nakanishi, S. Miyasaka, Y. Tokura, Large thermoelectric response of metallic perovskites: Sr 1− x La x TiO 3 (0<~ x<~ 0. 1), Phys. Rev. B 63 (11) (2001) 113104.
[11] H. Muta, K. Kurosaki, S. Yamanaka, Thermoelectric properties of reduced and La-doped single-crystalline SrTiO3, J. Alloys Compd. 392 (1-2) (2005) 306–309.
[12] F. Azough, A. Gholinia, D.T. Alvarez-Ruiz, E. Duran, D.M. Kepaptsoglou, A.S. Eggeman, Q.M. Ramasse, R. Freer, Self-Nanostructuring in SrTiO3: a novel strategy for enhancement of thermoelectric response in oxides, ACS Appl. Mater. Interfaces 11 (36) (2019) 32833–32843.
[13] Z. Lu, H. Zhang, W. Lei, D.C. Sinclair, I.M. Reaney, High-figure-of-merit thermoelectric La-doped A-site-deficient SrTiO3 ceramics, Chem. Mater. 28 (3) (2016) 925–935.
[14] J. Wang, B.-Y. Zhang, H.-J. Kang, Y. Li, X. Yaer, J.-F. Li, Q. Tan, S. Zhang, G.-H. Fan, C.-Y. Liu, Record high thermoelectric performance in bulk SrTiO3 via nano-scale modulation doping, Nano Energy 35 (2017) 387–395.
[15] J.U. Rahman, W.H. Nam, N. Van Du, G. Rahman, A.U. Rahman, W.H. Shin, W.-S. Seo, M.H. Kim, S. Lee, Oxygen vacancy revived phonon-glass electron-crystal in SrTiO3, J. Eur. Ceram. Soc. 39 (2-3) (2019) 358–365.
[16] D. Suh, D. Lee, C. Kang, I.-J. Shon, W. Kim, S. Baik, Enhanced thermoelectric properties of tungsten disulfide-multiwalled carbon nanotube composites, J. Mater. Chem. 22 (40) (2012) 21376–21381.
[17] L.-D. Chen, Z. Xiong, S.-Q. Bai, Recent progress of thermoelectric nano-composites, J. Inorganic Mater. 25 (6) (2010) 561–568.
[18] N.A. Heinz, T. Ikeda, Y. Pei, G.J. Snyder, Applying quantitative microstructure control in advanced functional composites, Adv. Funct. Mater. 24 (15) (2014) 2135–2153.
[19] P.R. Cantwell, M. Tang, S.J. Dillon, J. Luo, G.S. Rohrer, M.P. Harmer, Grain boundary complexions, Acta Mater. 62 (2014) 1–48.
[20] P.-a. Zong, X. Chen, Y. Zhu, Z. Liu, Y. Zeng, L. Chen, Construction of a 3D-rGO network-wrapping architecture in a Yb y Co 4 Sb 12/rGO composite for enhancing the thermoelectric performance, J. Mater. Chem. A 3 (16) (2015) 8643–8649.
[21] B. Feng, J. Xie, G. Cao, T. Zhu, X. Zhao, Enhanced thermoelectric properties of p-type CoSb 3/graphene nanocomposite, Journal of Materials Chemistry A 1 (42) (2013) 13111–13119.
[22] H. Ju, M. Kim, J. Kim, A facile fabrication of n-type Bi2Te3 nanowire/graphene layer-by-layer hybrid structures and their improved thermoelectric performance, Chem. Eng. J. 275 (2015) 102–112.
[23] J. Dong, W. Liu, H. Li, X. Su, X. Tang, C. Uher, In situ synthesis and thermoelectric properties of PbTe–graphene nanocomposites by utilizing a facile and novel wet chemical method, J. Mater. Chem. A 1 (40) (2013) 12503–12511.
[24] H. Chen, C. Yang, H. Liu, G. Zhang, D. Wan, F. Huang, Thermoelectric properties of CuInTe 2/graphene composites, CrystEngComm 15 (34) (2013) 6648–6651.
[25] J.U. Rahman, N. Van Du, W.H. Nam, W.H. Shin, K.H. Lee, W.-S. Seo, M.H. Kim, S. Lee, Grain boundary interfaces controlled by reduced graphene oxide in nonstoichiometric SrTiO 3-δ thermoelectrics, Sci. Rep. 9 (1) (2019) 1–12.
[26] O. Okhay, S. Zlotnik, W. Xie, K. Orlinski, M.J.H. Gallo, G. Otero-Irurueta, A.J. Fernandes, D.A. Pawlak, A. Weidenkaff, A. Tkach, Thermoelectric performance of Nb-doped SrTiO3 enhanced by reduced graphene oxide and Sr deficiency cooperation, Carbon 143 (2019) 215–222.
[27] C. Wu, J. Li, Y. Fan, J. Xing, H. Gu, Z. Zhou, X. Lu, Q. Zhang, L. Wang, W. Jiang, The effect of reduced graphene oxide on microstructure and thermoelectric properties of Nb-doped A-site-deficient SrTiO3 ceramics, J. Alloys Compd. 786 (2019) 884–893.
[28] Y. Lin, C. Norman, D. Srivastava, F. Azough, L. Wang, M. Robbins, K. Simpson, R. Freer, I.A. Kinloch, Thermoelectric power generation from lanthanum strontium titanium oxide at room temperature through the addition of graphene, ACS Appl. Mater. Interfaces 7 (29) (2015) 15898–15908.
[29] D. Srivastava, C. Norman, F. Azough, D. Ekren, K. Chen, M. Reece, I. Kinloch, R. Freer, Anisotropy and enhancement of thermoelectric performance of Sr 0.8 La 0.067 Ti 0.8 Nb 0.2 O 3− δ ceramics by graphene additions, J. Mater. Chem. A 7 (42) (2019) 24602–24613.

[30] P. Roy, V. Pal, T. Maiti, Effect of Spark Plasma Sintering (SPS) on the thermoelectric properties of SrTiO3: 15 at% Nb, Ceram. Int. 43 (15) (2017) 12809–12813.
[31] W.S. Hummers Jr, R.E. Offeman, Preparation of graphitic oxide, J. Am. Chem. Soc. 80 (6) (1958) 1339-1339.
[32] A.C. Ferrari, J. Robertson, Interpretation of Raman spectra of disordered and amorphous carbon, Phys. Rev. B 61 (20) (2000) 14095.
[33] S. Stankovich, D.A. Dikin, R.D. Piner, K.A. Kohlhaas, A. Kleinhammes, Y. Jia, Y. Wu, S.T. Nguyen, R.S. Ruoff, Synthesis of graphene-based nanosheets via chemical reduction of exfoliated graphite oxide, Carbon 45 (7) (2007) 1558–1565.
[34] J.-K. Lee, S. Lee, Y.-I. Kim, J.-G. Kim, B.-K. Min, K.-I. Lee, Y. Park, P. John, The seeded growth of graphene, Sci. Rep. 4 (2014) 5682.
[35] S. Wang, Y. Zhang, N. Abidi, L. Cabrales, Wettability and surface free energy of graphene films, Langmuir 25 (18) (2009) 11078–11081.
[36] P. Roy, V. Waghmare, T. Maiti, Environmentally friendly Ba x Sr 2− x TiFeO 6 double perovskite with enhanced thermopower for high temperature thermoelectric power generation, RSC Adv. 6 (60) (2016) 54636–54643.
[37] N. Wang, H. Chen, H. He, W. Norimatsu, M. Kusunoki, K. Koumoto, Enhanced thermoelectric performance of Nb-doped SrTiO3 by nano-inclusion with low thermal conductivity, Sci. Rep. 3 (2013) 3449.
[38] W. Wunderlich, H. Ohta, K. Koumoto, Enhanced effective mass in doped SrTiO3 and related perovskites, Phys. B 404 (16) (2009) 2202–2212.
[39] S. Lee, G. Yang, R.H.T. Wilke, S. Trolier-McKinstry, C.A. Randall, Thermopower in highly reduced n-type ferroelectric and related perovskite oxides and the role of heterogeneous nonstoichiometry, Phys. Rev. B 79 (13) (2009) 134110.
[40] L. Bjaalie, A. Janotti, B. Himmetoglu, C. Van de Walle, Turning SrTiO 3 into a Mott insulator, Phys. Rev. B 90 (19) (2014) 195117.
[41] Y. Kumar, R. Choudhary, S. Sharma, M. Knobel, R. Kumar, Strain dependent stabilization of metallic paramagnetic state in epitaxial NdNiO3 thin films, Appl. Phys. Lett. 101 (13) (2012) 132101.
[42] J. Liu, M. Kareev, D. Meyers, B. Gray, P. Ryan, J. Freeland, J. Chakhalian, Metal-insulator transition and orbital reconstruction in Mott-type quantum wells made of NdNiO 3, Phys. Rev. Lett. 109 (10) (2012) 107402.
[43] N. Palina, L. Wang, S. Dash, X. Yu, M.B. Breese, J. Wang, A. Rusydi, Investigation of the metal–insulator transition in NdNiO 3 films by site-selective X-ray absorption spectroscopy, Nanoscale 9 (18) (2017) 6094–6102.
[44] L. Zhang, Z.-J. Tang, Polaron relaxation and variable-range-hopping conductivity in the giant-dielectric-constant material Ca Cu 3 Ti 4 O 12, Phys. Rev. B 70 (17) (2004) 174306.
[45] J.A. Bock, S. Trolier-McKinstry, G.D. Mahan, C.A. Randall, Polarization-based perturbations to thermopower and electronic conductivity in highly conductive tungsten bronze structured (Sr, Ba) Nb 2 O 6: Relaxors vs normal ferroelectrics, Phys. Rev. B 90 (11) (2014) 115106.
[46] T. Holstein, Studies of polaron motion: Part II. The “small” polaron, Ann. Phys. 8 (3) (1959) 343–389.
[47] R. Raffaelle, H.U. Anderson, D.M. Sparlin, P.E. Parris, Transport anomalies in the high-temperature hopping conductivity and thermopower of Sr-doped La (Cr, Mn) O 3, Phys. Rev. B 43 (10) (1991) 7991.
[48] H.-S. Kim, Z.M. Gibbs, Y. Tang, H. Wang, G.J. Snyder, Characterization of Lorenz number with Seebeck coefficient measurement, APL Mater. 3 (4) (2015) 041506.
[49] D. Chen, Y. Zhao, Y. Chen, B. Wang, H. Chen, J. Zhou, Z. Liang, One-step chemical synthesis of ZnO/graphene oxide molecular hybrids for high-temperature thermoelectric applications, ACS Appl. Mater. Interfaces 7 (5) (2015) 3224–3230.
[50] J. Callaway, Model for lattice thermal conductivity at low temperatures, Phys. Rev. 113 (4) (1959) 1046.
[51] E. Langenberg, E. Ferreiro-Vila, V. Leborán, A. Fumega, V. Pardo, F. Rivadulla, Analysis of the temperature dependence of the thermal conductivity of insulating single crystal oxides, APL Mater. 4 (10) (2016) 104815.
[52] L. Daniels, S. Savvin, M. Pitcher, M. Dyer, J. Claridge, S. Ling, B. Slater, F. Cora, J. Alaria, M. Rosseinsky, Phonon-glass electron-crystal behaviour by A site disorder in n-type thermoelectric oxides, Energy Environ. Sci. 10 (9) (2017) 1917–1922.
[53] H. Casimir, Note on the conduction of heat in crystals, Physica 5 (6) (1938) 495–500.
[54] V. Ambegaokar, Thermal resistance due to isotopes at high temperatures, Phys. Rev. 114 (2) (1959) 488.
[55] X. Shi, Y. Pei, G.J. Snyder, L. Chen, Optimized thermoelectric properties of Mo 3 Sb 7− x Te x with significant phonon scattering by electrons, Energy Environ. Sci. 4 (10) (2011) 4086–4095.
[56] G.A. Slack, Thermal conductivity of Ca F 2, Mn F 2, Co F 2, and Zn F 2 crystals, Phys. Rev. 122 (5) (1961) 1451.